Compressive strength of delaminated aerospace composites

By Richard Butler*, Andrew T. Rhead , Wenli Liu and Nikolaos Kontis
Composites Research Unit, Department of Mechanical Engineering,
University of Bath, Claverton Down, Bath, BA2 7AY UK.

An efficient analytical model is described that predicts the value of compressive strain below which buckle-driven propagation of delaminations in aerospace composites will not occur. An extension of this efficient Strip model which accounts for propagation transverse to the direction of applied compression is derived. In order to provide validation for the Strip model a number of laminates were artificially delaminated producing a range of thin anisotropic sub-laminates made up of 0°, $\pm 45^o$ and 90° plies that displayed varied buckling and delamination propagation phenomena. These laminates were subsequently subject to experimental compression testing and non-linear Finite Element Analysis (FEA) using cohesive elements. Comparison of Strip model results with those from experiments indicates that the model can conservatively predict the strain at which propagation occurs to within 10% of experimental values provided (i) the thin-film assumption made in the modelling methodology holds and (ii) full elastic coupling effects do not play a significant role in the post-buckling of the sub-laminate. With such provision, the model was more accurate and produced fewer non-conservative results than FEA. The accuracy and efficiency of the model make it well suited to application in optimum ply-stacking algorithms to maximise laminate strength.

Keywords: delamination; composites; compression; impact; propagation

1. Introduction

Carbon fibre reinforced plastics (CFRP) have the potential to radically reduce the weight of any structure in which they are employed. This is a consequence of their favourable strength and stiffness properties and the way in which these can be tailored to give different directional properties. However, even in aircraft such as the Boeing 787 and the Airbus A350 this weight saving may not be fully exploited. There are a number of reasons for this; one of the most significant being Barely Visible Impact Damage (BVID), a topic which has been the subject of substantial research effort in the field of composites for the last thirty years. When layered structures are impacted their structural properties can be severely reduced. Often this is a consequence of the formation of hidden delaminations. This problem becomes acute when damaged structures are placed under compressive loads which tend to cause thin, outer sub-laminates to buckle locally, creating a mechanism for delamination propagation, and premature failure. Hence aerospace regulations specify that such laminates must tolerate BVID without failure for ultimate levels of load, where ultimate is usually 50% above limit load. This typically reduces allowable strains to around 4,500 µstrain. In some applications this gives component strengths that are less than half of the equivalent values for aluminium.

The analysis of delamination propagation following buckling deformation of a sub-laminate is complicated by the occurrence of a mix of peeling (Mode I), shearing (Mode II) and tearing (Mode III) actions along the delamination perimeter. Hence, non-linear Finite Element analyses employing interface elements or virtual crack closure techniques (VCCT) are the methods usually adopted, for example see [1-4]. However, such methods are complex, requiring large computational effort and do not lend themselves to understanding the mechanisms that promote or reduce damage tolerance across a range of laminates. It is therefore crucial that simplified methods are developed to capture such mechanisms and thus provide engineering tools to improve damage tolerance during optimum laminate design.

The authors have previously derived a simple, semi-numerical, fracture mechanics model to predict critical values of applied strain at which such buckle-driven propagation of delamination occurs [5]. This work extended the principles of Strain Energy Release Rate (SERR) considered by others [6-8] for propagation of a delamination, to the case of a two-dimensional, anisotropic plate containing a delamination. In this paper the authors present a new extension to this extremely efficient Strip model [5]. The model assumes simplified components of bending and membrane (strain) energy in the post-buckled, thin sub-laminate created by the delamination and is based on the concept of establishing an equivalent Mode I approximation of the actual, mixed-mode SERR. The current paper clarifies the underlying methodology of the previous work [5] and extends it by improving the accuracy of the Strip model for transverse growth, perpendicular to the loading direction. This is accomplished by considering the direction of maximum axial stiffness in the thin sub-laminate in either the loading or transverse directions.

The new Strip model methodology and its simplifying assumptions are validated against the results of a series of new experiments and Finite Element analyses on laminates containing a single artificial circular delamination producing different types of anisotropy in the thin, buckled sub-laminate. The experiments were monitored using a high speed digital image correlation (DIC) system which produces plots of full field deformation and principal strains so that the occurrence of critical buckling as well as the onset, mode and stability of propagation can be pin-pointed.

2. Modelling methods

(a) Strip model: the concept of equivalent energy release

(i) Initial post-buckling

Hunt *et al.* [9] showed that a thin sub-laminate created by near-surface delamination of an isotropic strut placed under compressive load can buckle to open the delamination. A transition from delamination opening to closing occurs for deeper delaminations where the point of transition defines the critical depth. This depth is dependent on the effective length of the strut compared with the length of the delamination. When the strut has an effective length that is twice the delamination length, the critical depth occurs at about 25% of total thickness.

For the laminated plates that follow, and for most delaminations that have been caused by impact damage, the delaminations from which propagation will occur are at depths less than 25% of total thickness. Furthermore, the anti-buckling guides used in the tests described below create effective lengths less than twice the delamination

length. Hence these delaminations open under compressive load, and the failure is triggered by this opening (sub-laminate buckling).

(ii) One-dimensional propagation

The proposed model assumes that all post-buckled energy in the thin sub-laminate available for propagation of the delamination is in the form of bending energy, i.e. there is no membrane energy available after buckling, meaning that there is no release of energy associated with post-buckled stiffness.

Initially, a one-dimensional, thin-film sub-laminate buckling above a flat substrate, see figure 1, is developed so that the principles can later be extended to the more complicated two-dimensional case. Thin-film conditions are assumed so that no bending energy is released from the substrate during propagation.
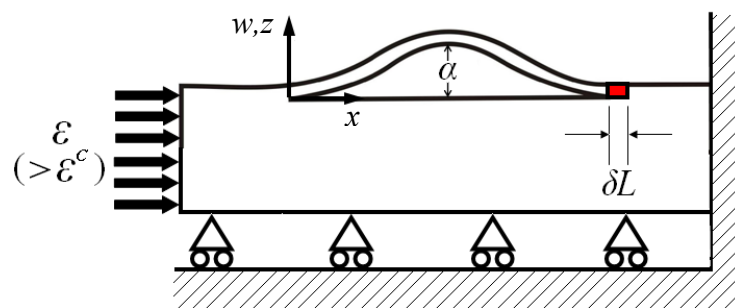

Figure 1. One-dimensional post-bucking of a thin sub-laminate of undeformed length L and thickness t above a flat substrate.

Applying a sinusoidal buckling displacement

$$w = \frac{\alpha}{2}(1 - \cos\frac{2\pi x}{L})$$ (2.1)

The bending energy U_B in the buckled sub-laminate, which has bending rigidity EI, is given by

$$U_B = \frac{EI}{2}\int_0^L\left(\frac{\partial^2 w}{\partial x^2}\right)^2 dx = \pi^4 EI\frac{\alpha^2}{L^3}$$ (2.2)

And the end shortening of the sub-laminate is taken as

$$\Delta = \frac{1}{2}\int_0^L\left(\frac{\partial w}{\partial x}\right)^2 dx = \frac{\pi^2}{4}\frac{\alpha^2}{L}$$ (2.3)

Hence the potential energy V of the force P applied to the thin sub-laminate is

$$V = -P\Delta$$ (2.4)

For equilibrium, according to the principle of minimum potential energy

$$\frac{\partial U_B}{\partial \alpha} + \frac{\partial V}{\partial \alpha} = 0 \tag{2.5}$$

Substituting equations (2.2)-(2.4) into equation (2.5) we obtain the critical buckling load of the sub-laminate

$$P^C = \frac{4\pi^2 EI}{L^2} \tag{2.6}$$

For unit width and thickness t of sub-laminate, the critical strain is then

$$\varepsilon^C = \frac{P^C}{Et} \tag{2.7}$$

If we ignore any post-buckling stiffness and assume that the end shortening of equation (2.3) is equal to the applied end-shortening following buckling then

$$L(\varepsilon - \varepsilon^C) = \frac{\pi^2 \alpha^2}{4L} \tag{2.8}$$

From equation (2.2), the bending energy in the buckle can be re-written

$$U_B = 4\pi^2 EI \frac{\left(\varepsilon - \varepsilon^C\right)}{L} \tag{2.9}$$

The rate at which bending energy is released as the delamination propagates is

$$-\frac{\partial U_B}{\partial L} = \varepsilon^C Et \left(\varepsilon - \varepsilon^C + L\frac{d\varepsilon^C}{dL} \right) \tag{2.10}$$

Assuming that there is no post-buckled stiffness in the sub-laminate, we add the membrane energy released by the small unbuckled element δL in figure 1 as the delamination propagates.

$$U_{M,1} = \frac{Et}{2} \int_0^{\delta L} \varepsilon^2 dx \tag{2.11}$$

Similarly, the membrane energy retained by the element δL as it becomes part of the buckled region following propagation is given by

$$U_{M,2} = \frac{Et}{2} \int_0^L (\varepsilon^C)^2 dx \tag{2.12}$$

The difference of equations (2.11) and (2.12) gives the energy available for release and therefore the rate of membrane energy released during propagation of element δL,

$$\frac{\partial U_M}{\partial L} = \frac{Et}{2}\left(\varepsilon^2 - \left(\varepsilon^C\right)^2 - 2\varepsilon^C L \frac{d\varepsilon^C}{dL}\right) \qquad (2.13)$$

This allows for the fact that only the membrane energy above the critical strain is available for release from the un-buckled element.

Adding together the bending and membrane energies released as a result of propagation of the buckled sub-laminate we obtain the following Strain Energy Release Rate (SERR)

$$G = \frac{Et}{2}\left(\varepsilon - \varepsilon^C\right)\left(\varepsilon + 3\varepsilon^C\right) \qquad (2.14)$$

Note that the final terms of equations (2.10) and (2.13) cancel, meaning that the result is unchanged if we assume no variation of ε^C with L [5]. Equation (2.14) was obtained by Chai et al [6] and requires the assumption that there is no post-buckled stiffness in the thin sub-laminate. If a further assumption is made that any Mode II contribution is ignored and a pure Mode I peeling action is assumed at the tip of the delamination, a Mode I propagation criterion can be applied. The Mode II contribution may actually be significant but since the energy required for Mode I fracture is always significantly less than that required for Mode I fracture the Mode I criterion is conservative. Hence, propagation is assumed to occur when G_{IC}, the critical SERR for the material in which the delamination occurs, is reached ($G = G_{IC}$), at which point the applied strain reaches its threshold propagation value ($\varepsilon = \varepsilon_{th}$), and

$$G_{1C} = \frac{Et}{2}\left(\varepsilon_{th} - \varepsilon^C\right)\left(\varepsilon_{th} + 3\varepsilon^C\right) \qquad (2.15)$$

Re-arranging for the threshold strain gives

$$\varepsilon_{th} = \varepsilon^C\left(\sqrt{4 + \frac{2G_{IC}}{Et\left(\varepsilon^C\right)^2}} - 1\right) \qquad (2.16)$$

Note that, although the critical buckling strain depends on the delamination length, the SERR is independent of this length.

(iii) Two-dimensional buckling and propagation

As above, the two-dimensional sub-laminate is assumed to buckle as a thin film above a flat substrate, see figure 2. In the case considered here we assume that out-of-plane rotation and out-of-plane displacement are prevented along the circular perimeter of the delamination and that the sub-laminate is subject to forces arising from compatibility with the full laminate (substrate). These forces are calculated from the full laminate stiffness matrix in the following way. Assuming zero curvature in a balanced and symmetric parent laminate (displaying neither extension/shear coupling nor in-plane/out-of-plane coupling), the loads acting on the thin sub-laminate $\{N\}_{SL}$

are determined by obtaining the strain $\{\varepsilon\}_L$ of the full parent laminate when unit axial strain is applied. $\{N\}_{SL}$ is then calculated, by assuming compatibility of strain from,

$$\{N\}_{SL} = [A]_{SL}\{\varepsilon\}_L \tag{2.17}$$

i.e.

$$\begin{Bmatrix} N_x \\ N_y \\ N_{xy} \end{Bmatrix}_{SL} = \begin{bmatrix} A_{11} & A_{12} & A_{13} \\ A_{12} & A_{22} & A_{23} \\ A_{13} & A_{23} & A_{33} \end{bmatrix}_{SL} \begin{Bmatrix} \varepsilon \\ -\nu\varepsilon \\ \gamma_{xy} \end{Bmatrix}_L \tag{2.18}$$

where $[A]_{SL}$ is the in-plane (membrane) stiffness matrix of the thin sub-laminate and ν, the effective Poisson's ratio of the full laminate.
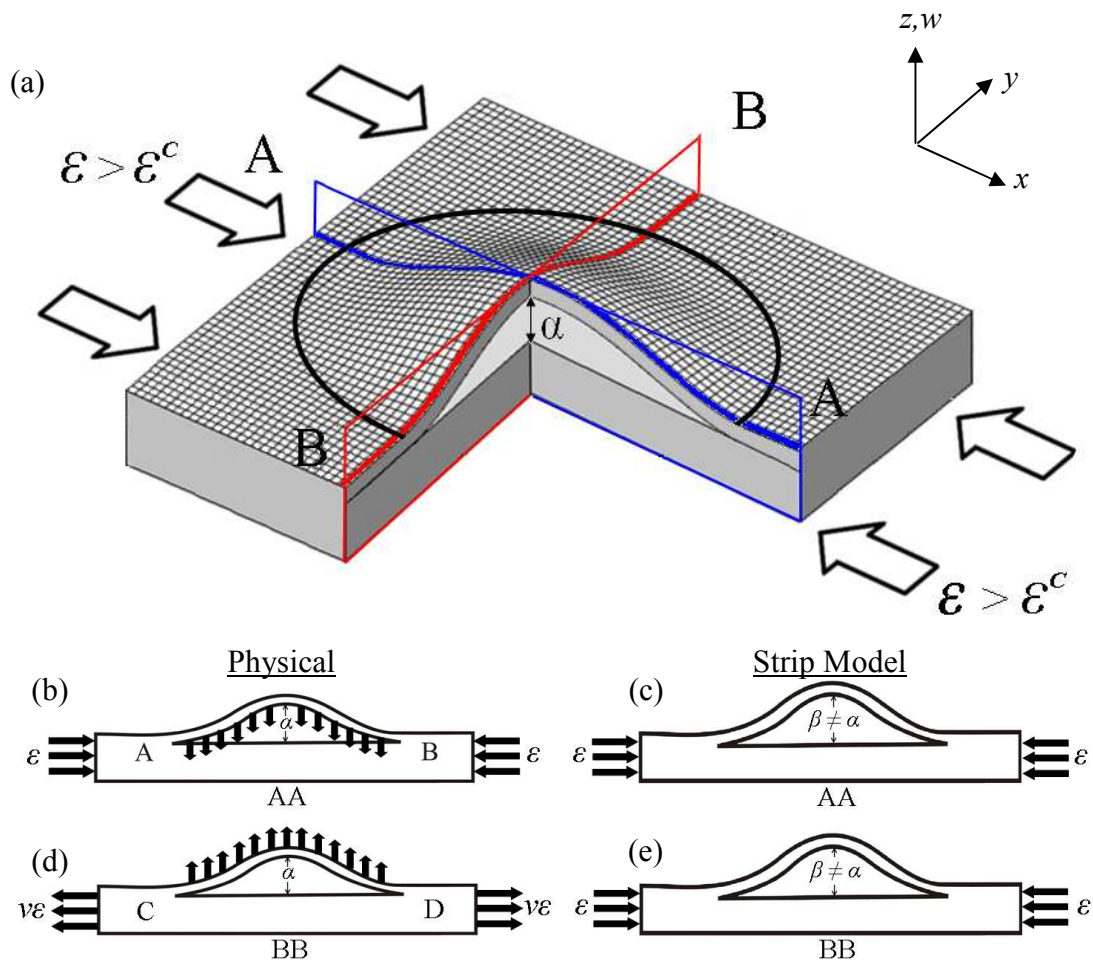

Figure 2. Post-buckling of thin circular sub-laminate subject to uni-axial compressive strain ε. (a) Isometric cutaway showing compressive strip (AA) and tensile strip (BB), (b) section of compressive strip and (c) Strip model equivalent. (d) Section of tensile strip and (e) Strip model equivalent.

Note that although uni-axial strain is applied to the full laminate (shear strain, $\gamma_{xy} = 0$), equation (2.17) may result in bi-axial load and shear being applied to

the thin sub-laminate. Note also that equation (2.17) assumes that positive strains and loads are compressive.

In order to calculate the critical value of applied axial strain ε^C an extremely efficient, infinite strip model [10] is used in the results that follow. The values of critical strain could also be determined using Finite Element software, as is shown later for comparison, but the use of the infinite strip model is much more efficient. This approach divides the circular sub-laminate into a number of strips of equal width while applying compatibility and equilibrium along the connecting nodal lines. The differential equations representing periodic buckling deformation of these strips are then solved exactly to develop a transcendental eigenvalue problem [11]. Points at which these nodal lines intersect with the circular delamination boundary are restraining points where the sinusoidal wavelengths are combined to match the boundary using energy minimisation principles [12]. For the results presented later, 6 equal width strips are used with 12 constrained nodes at the junction of these strips and the circular boundary, see [13]. The thin, two dimensional sub-laminate can be unbalanced and asymmetric, which can give rise to fully populated matrices for in-plane membrane stiffness $[A]_{SL}$, out-of-plane bending stiffness $[D]_{SL}$, and coupling stiffness $[B]_{SL}$. However, VICONOPT buckling analysis is fully general, and can analyse such laminates.

Analysis of the post-buckling behaviour of the sub-laminate requires full non-linear modelling. The behaviour is schematically described here in order to explain the actual mechanism by which strain energy is released as the delamination propagates in two dimensions. This will become useful when we make simplifying assumptions about the SERR. Considering the two orthogonal strips shown in figure 2, we see that the post-buckled compressive strip (figure 2(b)) is restrained by downward forces representing the effect of orthogonal tensile strips, e.g. figure 2(d), that are being stretched to accommodate the post-buckling deformation. The combined effects give rise to mixed mode conditions all along the delamination front [14]. As above, we isolate the Mode I (peeling) effect by assuming that all strain energy available for propagation is in the form of bending energy which is then released by a peeling mechanism, so that the (transverse) orthogonal strips are not assumed to develop any tensile components. This means that, during post-buckling, radial compression is assumed to act, and that the sub-laminate has no membrane stiffness following buckling, as illustrated in figures 2(c) and (e). As in the one-dimensional case, this does not represent the mixed mode system but assumes that all energy is available for release via a peeling mechanism in the form of (i) bending energy in the thin sub-laminate and (ii) membrane energy (above ε^C) in the unbuckled perimeter of the delamination. In actual fact, the Mode I contribution must be less than this since the two-dimensional shape has post-buckled stiffness due to the development of tensile stresses in the lateral direction. Hence, less membrane energy than is represented by equation (2.13) is actually released. However, it is expedient, with regard to producing a simple model, that ignoring these non-linear two-dimensional effects appears to have little influence on the prediction of threshold propagation strain for thin sub-laminates, as shown by comparison with the experimental and FEA results that follow.

Hence, this justifies the new concept of an equivalent Mode I energy criterion, replacing the need for a mixed mode expression and non-linear post-buckling analysis. The strain ε_{th}, at which propagation occurs is as above, i.e.

$$\varepsilon_{th} = \varepsilon^C \left(\sqrt{4 + \frac{2G_{1C}}{A_{nn,SL}(\varepsilon^C)^2}} - 1 \right) \tag{2.19}$$

where $A_{nn,SL}$ is the axial stiffness of the sub-laminate and

$$n = 1 \text{ when } A_{11,\,SL} > A_{22,\,SL}$$

or

$$n = 2 \text{ when } A_{22,\,SL} > A_{11,\,SL}$$

In the former case ($n = 1$), the longitudinal stiffness of the sub-laminate dominates and so propagation is assumed to initiate in the x-direction and SERR is calculated for this direction. In the latter case ($n = 2$), propagation initiates in the y-direction, we assume that pre-buckling compressive strain is applied in the longitudinal x-direction in order to find ε^C and that post-buckled compressive strain is applied in the transverse y-direction in order to develop the equivalent Mode I energy release in that direction. This assumes that the sub-laminate buckles due to the actual applied strain but all subsequent strain energy is developed in the direction of greater axial stiffness. In actual fact, transverse propagation is dominated by Mode II effects but by applying transverse compressive strain to the sub-laminate we do not allow post-buckled tension to develop and account for the *equivalent* Mode I requirement for propagation in that direction.

It is interesting to observe that, although the buckling strain is dependent on the shape of the delamination boundary, propagation appears to be independent of this shape, as in the one-dimensional case.

(b) Finite Element Analysis using cohesive elements

In order to provide validation for the Strip model and to give further insight into the supporting experimental validation, the nonlinear Finite Element program ABAQUS [15] was applied to predict the strains required for sub-laminate buckling and delamination growth in the artificially delaminated laminates considered in the next section. The laminate was separated into three regions, with the interface zone, which is populated with cohesive elements, being sandwiched between the thin sub-laminate and the thick base laminate, see figure 3. Four-noded shell elements (S4) were used in the sub-laminate and base to account for any through-thickness shear deformation that may arise in the test coupons. In addition, the area around the delamination front was finely meshed to ensure solution convergence and to accurately capture delamination initiation and growth. Note that the three layers have the same mesh design and density, see figure 4, and that the nodes on the bottom edge had clamped boundary conditions. Compression was applied as a uniform displacement in the x-direction along the top edge of the mesh where all other displacements and rotations are fixed. Moreover, the nodes between the circular edge of the anti-buckling guide described below and the four straight edges were constrained to prevent out-of-plane displacement as is the function of the anti-buckling guide in the physical experiments described in §3(a). In order to prevent overlap of the sub-laminate and base thus ensuring feasible solutions, a surface-to-surface contact constraint was applied in the delamination zone. Eight-noded 3D cohesive elements were used at the interface between the base and sub-laminates, in order to predict delamination propagation. The cohesive layer was composed of zero thickness volumetric elements, which have the following definitions.
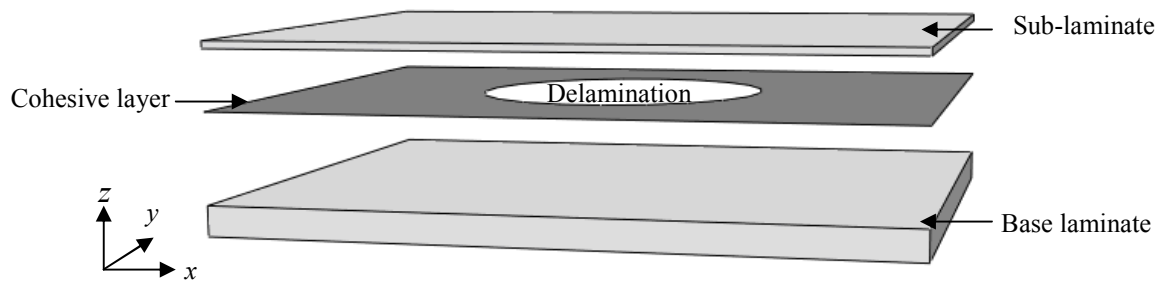
Figure 3. Schematic of Finite Element model, showing an exploded view of the thin sub-laminate (4-noded shell composite element (S4)), cohesive layer (3D 8-noded cohesive element layer (COH3D8)) and base laminate (S4).
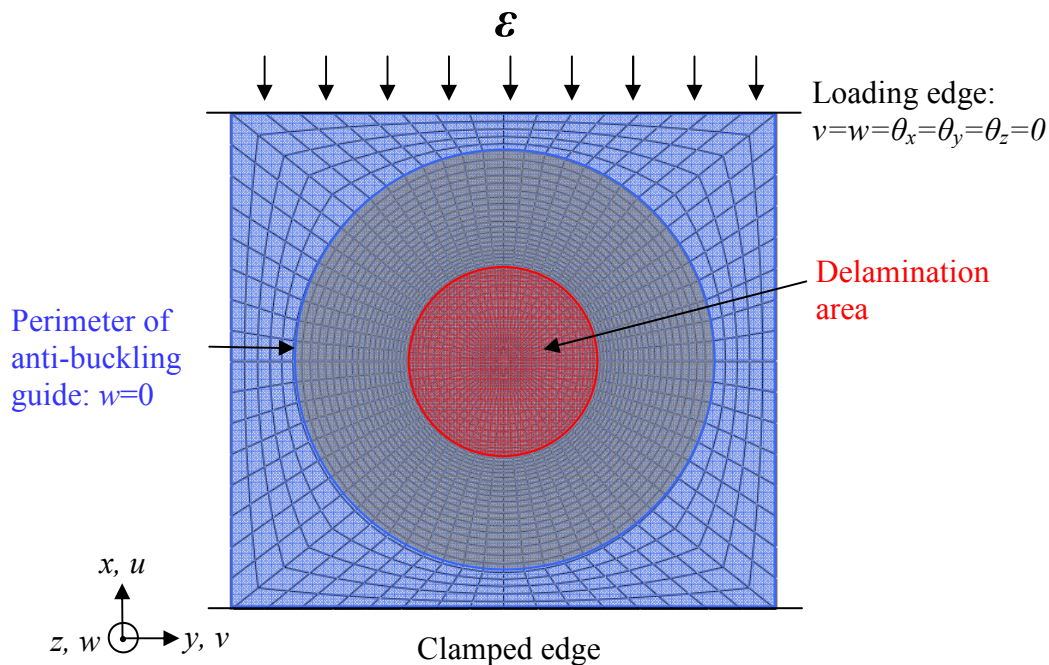

Figure 4. FE mesh, showing region of delamination and boundary conditions. The anti-buckling guide restrains the region outside the circle.

Stiffness is defined to relate the stress to the relative displacement at the interface. This parameter was chosen such that the value was large enough to ensure that the sub-laminate and base were well bonded prior to damage growth and small enough not to cause convergence problems. Three stiffness parameters can be defined in terms of peeling, shearing and tearing components, i.e. Modes I, II and III. The critical interlaminar material strength for each fracture mode was defined using a traction-separation law. For pure Mode I loading, material damage occurs once the interfacial normal stress reached its maximum interlaminar tensile strength, following which the stiffness was gradually reduced to zero. Under pure Mode I, II or III loading, the onset of damage at the interface can be determined simply by comparing the stress components with their respective maximum. However, under mixed mode loading, damage onset may occur before any of the individual stress components reaches their respective maximum value. Therefore, a damage initiation criterion was

defined to predict this mixed mode fracture. In this study, it was assumed that delamination initiation could be predicted using the quadratic failure criterion [1]. A damage propagation criterion, based on fracture energy, was defined to predict delamination growth under mixed-mode conditions. Here the energy-based Benzeggagh-Kenane law [16], which is the simplest to implement and most commonly used, was employed to predict delamination growth. The total critical energy release rate G_{TC} is given by,

$$G_{TC} = G_{IC} + \left(G_{IIC} - G_{IC}\right)\left(\frac{G_{II} + G_{III}}{G_I + G_{II} + G_{III}}\right)^{\eta}$$

(2.20)

where η is an empirical parameter derived from mixed-mode tests, G_{IC}, G_{IIC} and G_{IIIC} are critical energy release rates for respectively pure Mode I, II and III and G_I, G_{II} and G_{III} are the corresponding values determined from analysis. According to the criterion, the damage growth occurs when the total energy $G_I+G_{II}+G_{III} \geq G_{TC}$. Within the ABAQUS model, there are two stages involved in propagation. The first stage is delamination initiation at which the nodes at the delamination front start to separate, the second stage is delamination propagation in which entire cohesive elements fail and are removed.

3. Results

In order to test the applicability of the Strip model, a series of experimental and FEA test cases were considered. Experimental validation consisted of a series of compression tests on laminates constructed from unidirectional Carbon Fibre Reinforced Plastic (CFRP) layers. Each laminate was designed to display local sub-laminate buckling and propagation behaviour in order to provide benchmark results for the Strip model. This was achieved by employing non-stick circles of polytetrafluoroethylene (PTFE) at a single interface within each laminate. A range of examples, see table 1, were created by varying the degree of anisotropy displayed by the thin sub-laminate above the PTFE insert which is dependent on the number and orientation of plies making up the sub-laminate. Note that positive fibre orientations are defined as being clockwise with respect to the applied load direction (x-axis). Similarly for the FEA test cases a model was constructed using shell and cohesive elements, as explained above. This FEA model incorporated an anti-buckling guide in order to mimic the physical experiments as closely as possible. Eight so-called quasi-isotropic laminates, each having equal percentages of CFRP plies with fibres aligned at 0°, $+45^o$, -45° or 90° to the direction of applied load were manufactured from 0.25mm thick Hexcel T700GC/M21 pre-preg CFRP layers which have material properties $E_{11} = 136$ GPa, $E_{22} = 8.9$ GPa, $G_{12} = 4.5$ GPa, $v_{12} = 0.35$ and $G_{IC} = 550$ J/m^2. Sequences of layers that make up the laminates are given in table 1. Note that the full laminate stacking sequences are balanced and symmetric and thus negate the occurrence of the coupling effects described in the text above equation (2.17). During manufacture, PTFE circles 0.0125mm thick and 39mm in diameter were placed between selected layers in the laminates to produce areas where adhesion would be prevented i.e. artificial delaminations. Through-thickness positions of these inserts are given in table 1 by indicating the thin sub-laminate created. The test coupons will subsequently be referred to using the sub-laminate stacking sequence. Note that coupons with sub-laminates containing more than one 90° ply have artificial

delaminations at deeper interfaces than the other coupons as modeling indicated that a $[90_2]$ sub-laminate would have a delamination buckling strain that was too high to induce failure as a consequence of propagation following local sub-laminate buckling.

Table 1. Stacking sequences of laminates and thin sub-laminates for test coupons.

Laminate (delamination indicated by //)	Sub-laminate
$[\mathbf{0_2}//45/-45/90/45/-45/90_2/-45/45/90/-45/45/0_2]$	$[0_2]$
$[\mathbf{45_2}//-45_2/90/0/90/0_2/90/0/90/-45_2/45_2]$	$[45_2]$
$[\mathbf{45/-45}//0_2/-45/90/45/90_2/45/90/-45/0_2/-45/45]$	$[45/-45]$
$[\mathbf{90/0/90}//45/-45/45/-45/0_2/-45/45/-45/45/90/0/90]$	$[90/0/90]$
$[\mathbf{0/90_2}//45/-45/45/-45/0_2/-45/45/-45/45/90_2/0]$	$[0/90_2]$
$[\mathbf{90_2/0}//45/-45/45/-45/0_2/-45/45/-45/45/0/90_2]$	$[90_2/0]$
$[\mathbf{0_2/90}//45/-45/45/-45/90_2/-45/45/-45/45/90/0_2]$	$[0_2/90]$
$[\mathbf{0/45}//0/-45/90/45/-45/90_2/-45/45/90/-45/0/45/0]$	$[0/45]$

(a) Experimental test setup

Prior to compression testing, laminates were cut into coupons 210mm long by 100mm wide by 4mm thick and placed in a compression fixture with an integrated circular anti-buckling guide of internal diameter 85mm in order to prevent buckling outside this circle, see figure 5. Tests consisted of applying axial compression under displacement control at 0.1 mm/min until local propagation and/or global failure occurred. The faces of the coupons nearest the PTFE inserts were covered in a random speckle pattern to allow buckling modes and failure sequences to be visualised (following post-processing) using a Digital Image Correlation (DIC) system. This system employs a pair of stereo cameras to produce plots of out-of-plane displacement or variation in surface strain in the principal load direction relative to a reference image taken under zero load. As verification of 'far-field' strain for the DIC system and to ensure specimens were correctly aligned, strains were recorded throughout the tests by two pairs of vertically aligned back-to-back strain gauges. For each experiment, one pair of gauges were located inside but as close as possible to the anti-bucking guide on a vertical line through the centre of the circular PTFE insert and similarly the second pair were located inside but as close as possible to the anti-bucking guide on a horizontal line through the centre of the PTFE insert. See figure 6 for a schematic diagram of strain gauge placement for the $[45_2]$ laminate.
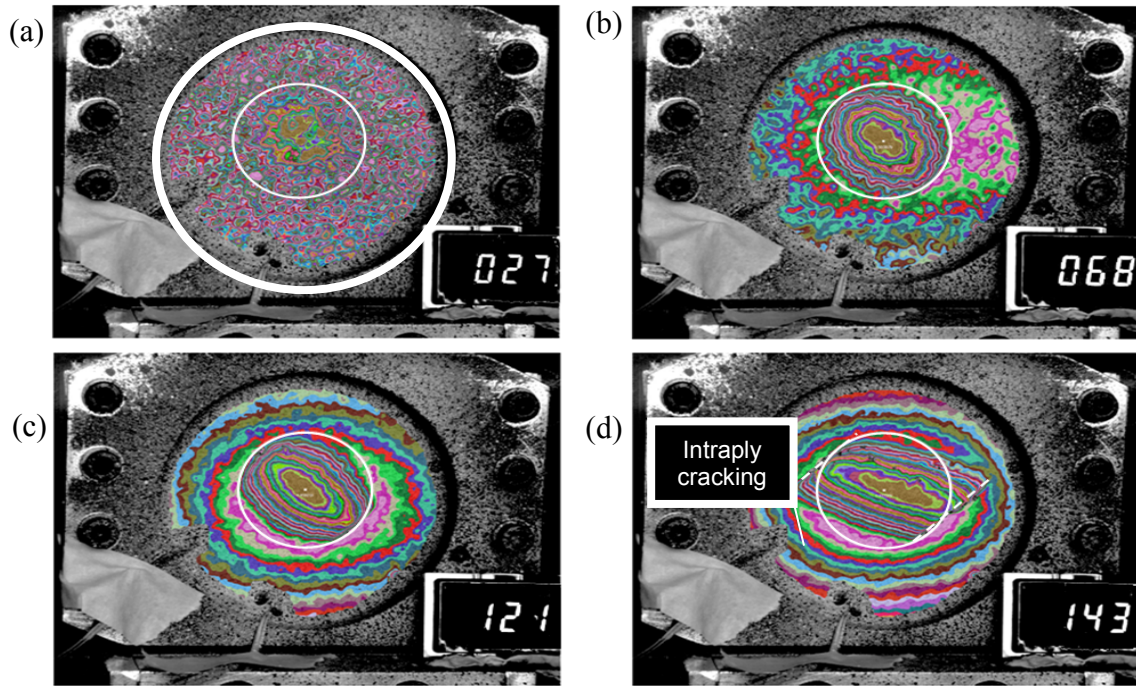
Figure 5. DIC images of the [45$_2$] coupon with 39mm white inner circle highlighting the position of the original delamination and 85mm white outer circle in (a) indicating the anti-buckling guide. (a) Initial locally buckled state (1600 µstrain), (b) fully buckled state (3740 µstrain), (c) propagated state (7200 µstrain) and (d) propagated state at approximately 8400 µstrain showing damage growth direction. The load is applied vertically and the corresponding LED load levels are shown in kN.
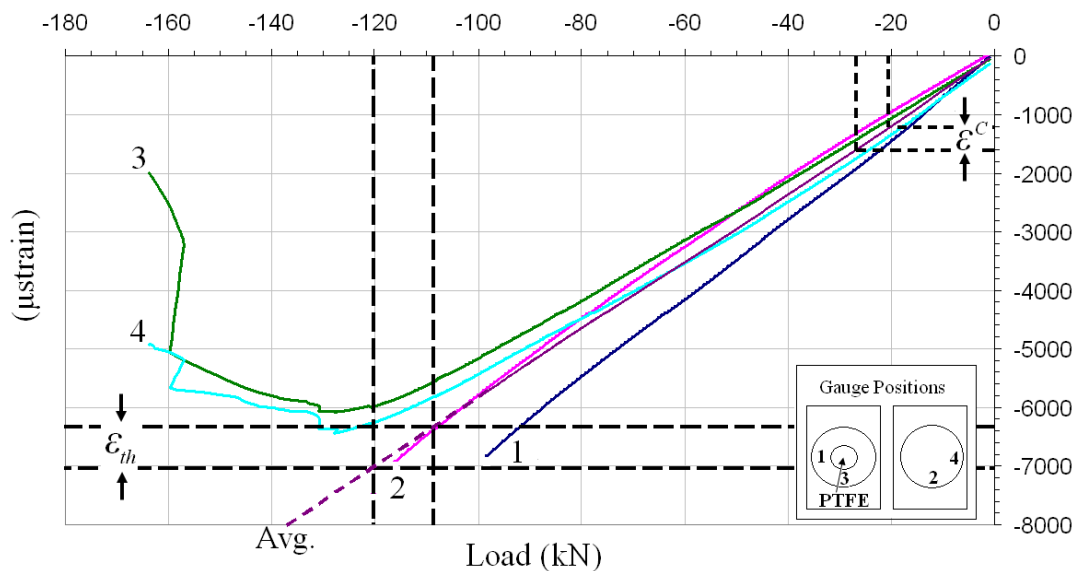

Figure 6. Strain vs. load for the [45$_2$] coupon showing individual strain gauge data and average strain. Buckling and initial propagation are indicated by horizontal and vertical dotted lines.

(b) Experimental Results

Results from the experimental tests are given in table 2. Experimental strains for local buckling and propagation are determined from a combination of load-strain plots (figure 6) and DIC images (figure 5). Unless noted otherwise, for all DIC images colours indicate changing out of plane displacement from an unloaded reference state. The DIC images and load-strain plots were linked by the load output of the compression test machine. The occurrence of propagation was detected by fitting a circle of diameter equal to the PTFE insert (using the internal anti-buckling guide diameter as a reference) around the fully formed buckle on a DIC image then visually determining when the local buckle had spread outside of this circle, see figures 5 (b) and (c). Using the LED load readout, propagation was correlated with the average of the four strain gauge readings on the respective load-strain plot to determine an experimental strain for initiation of propagation. The average of the four strain gauge readings was used as it accounts for losses in stiffness during the test.

Table 2. Buckling and propagation strains for the delaminated coupons described in table 1. Init./Prop. denotes initiation and propagation for the FEA results, see §3 (c).

Sub-laminate	ε^C Buckling (µstrain)			ε_{th} Propagation (µstrain)		
	Experiment	FEA	Strip model	Experiment	FEA (Init./Prop.)	Strip model
[0$_2$]	1250*	619	682	3540	3583 / 4545	3551
[45$_2$]	1200-1620	1534	1617	6310-7050	7862 / 8250	6264
[45/-45]	3010*	687	807	6700	7350 / 7820	6567
[90/0/90]	2630-3250*	1843	1898	3950-4260	3655 / 4227	3574
[0/90$_2$]	2340/1250†	2075	2164	3700-4280	3806 / 4727	3690
[90$_2$/0]	2800-3730*	2052	2164	3730	3811 / 5232	3690
[0$_2$/90]	1060-1470	1183	1262	2650	2838 / 3600	3419
[0/45]	400-600	481	511	2500-2700	3035 / 5000	4542

* Delayed experimental buckling due to adhesion.
† Results for first/second loading.

(i) Local buckling

Local buckling manifests itself as a change in gradient of the strain gauge curves (e.g., figure 6) and as an area with a high number of contours on the DIC images implying a rapidly changing out-of-plane displacement, see figure 5. However, these changes are often subtle as can be seen from figure 5(a) hence for a number of results in table 2 a range of buckling strains is given. The lower value coincides with when a buckle may have occurred on the DIC images and the upper value with when a buckle has definitely formed, contrast figures 5 (a) and (b). In general, local buckling mode-shapes for sub-laminates with no 0° plies had a smaller wavelength in the load direction resulting in a laterally elongated local buckle that did not fill the artificially delaminated area, see figure 7 (b). Note that the random pattern outside the local buckle seen in figure 5 (a) is partially a result of the system being unable to resolve the very small deflection changes occurring at low-levels of load in this area and partly due to the non-smooth surface of the sample which is a result of the surface finish.
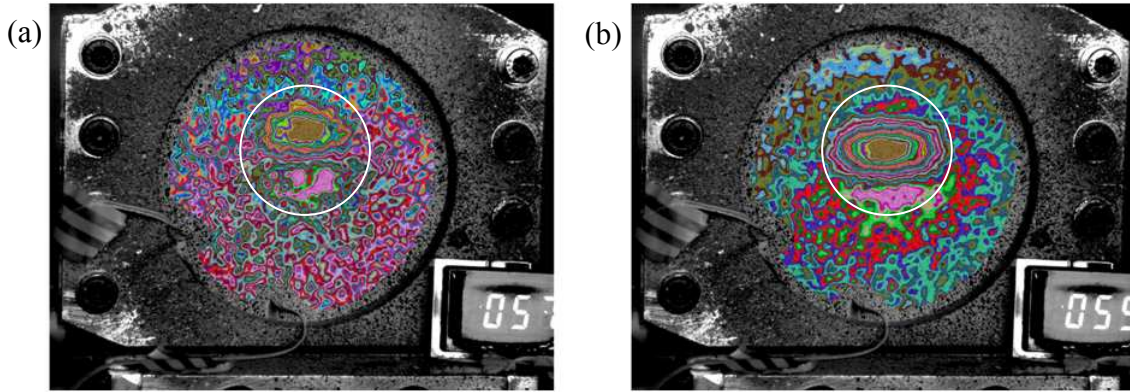
Figure 7. DIC images of the [0/90$_2$] coupon with a 39mm circle highlighting the position of the original delamination showing the buckled state immediately (a) before and (b) after a mode-shape change at approximately 3550 µstrain during the first loading .

During some experiments (marked with an asterix in table 2), despite the PTFE insert, some adhesion remained between the sub and base laminates. Hence, the sub-laminates for these coupons were not released until sufficient load had been applied to overcome this adhesion, resulting in an increased buckling strain. For the [45$_2$], [0/90$_2$], [0$_2$/90] and [0/45] sub-laminates, sufficient load was applied to release the sub-laminate prior to propagation after which loading was removed and the test reset. Thus buckling occurred for these tests without adhesion. In the case of the [0/90$_2$] coupon, no adhesion between the PTFE insert and sub-laminate occurred. During initial loading of this coupon (see table 2), a loud noise was mistaken for a release of the sub-laminate and the test was reset. DIC images taken during the initial test, identified that the loud noise was due to a sudden change in local buckling mode shape, see figures 7 (a) and (b). This so-called mode jump caused intra-ply cracking (between fibres in a ply) which resulted in local buckling in the second test bypassing the first buckling modeshape and instead exhibiting the second modeshape at a lower level of strain. This accounts for the discrepancy between buckling strains in table 2. Changes in local buckling modeshape were also noted in the [0$_2$/90] and [0/45] sub-laminates although in both these cases local buckling mode jumps coincided with a global buckling/bending event. The occurrence of global bending or buckling phenomena can be seen as wider contours in figure 5 in comparison to the thin contours and hence steep gradient changes that represent local buckling. Figures 8 (a) and (b) show that as the load increased significant global deformation occurred for [0$_2$/90] sub-laminate.

(ii) Propagation

Propagation was deemed to have occurred once the buckle spread outside a 39mm diameter circle centred at the point of greatest out-of-plane deflection, contrast figures 5 (b) and (c). This propagation was correlated with the corresponding load - strain plot where it was generally seen as a discontinuity in the strain gauge curves, see figure 6 where multiple propagation events are evident. However, as for local buckling, if growth occurred slowly it was not always possible to pinpoint when propagation occurred. Slow growth can occur as a stiffness change rather than a discontinuity on the load-strain plots. Thus for some cases in table 1 a range of propagation strains is given. The direction of propagation was influenced to a greater or lesser extent by each of the following; the direction of greatest sub-laminate stiffness, global

buckling/bending and the direction of the fibres in the bottom ply of the sub-laminate. If the base laminate were to remain completely flat, it is likely that the direction of propagation would be mostly influenced by the maximum stiffness direction of the sub-laminate and bottom ply fibre direction. However, most laminates displayed global buckling/bending which encouraged propagation to occur transverse to the load (see figure 8) and some laminates were influenced by the direction of the fibres in the bottom ply of the sub-laminate which encouraged growth parallel to the bottom ply fibre direction. This is because growth perpendicular to the fibre direction was inhibited by intraply cracking. Figure 5 shows how the three mechanisms combine to affect the direction of propagation in the $[45_2]$ laminate. Initiation of propagation occurred at a point on the perimeter of the PTFE insert away from the direction of the greatest sub-laminate stiffness at angle of approximately 60° (figure 5(c)) due to the influence of global buckling/bending and then subsequently propagates in the 45° direction as intraply cracking prevents growth in any other direction.
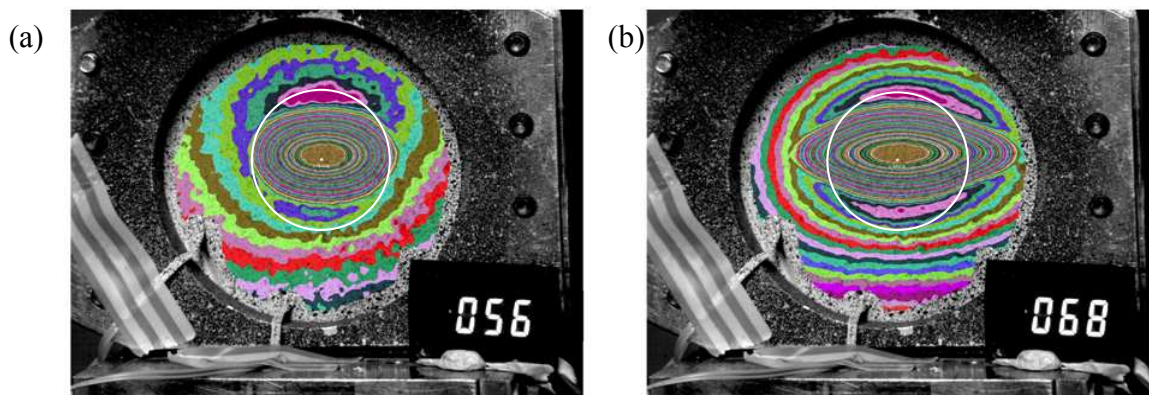
(a)　　(b)

Figure 8. DIC images of the $[0_2/90]$ sub-laminate with 39mm circle highlighting the position of the original delamination showing the propagated state at approximately (a) 2650 µstrain and (b) 3300 µstrain.

Intraply cracking was noted in sub-laminates having two plies of identical orientation on their upper surface, see figure 5. In these cases the intraply cracks drove the direction of growth as they prevented delamination propagation occurring perpendicular to the fibre direction. In the [90/0/90] and $[0_2/90]$ sub-laminates, delamination growth occurred at the artificially delaminated interface but it was not confined to this interface. Instead, following initial propagation at the artificially delaminated interface, intraply cracking allowed growth to transfer to the second ply interface in the sub-laminate. Although this is an interesting phenomenon, it occurred following initial propagation and so is outside the capabilities of the Strip and FEA models and hence is not discussed further here. Similar mechanisms have been recorded by Greenhalgh and Singh [17].

(c) Finite Element Results

The parameters used for cohesive elements within the FE analyses are summarised in table 3 and table 2 gives buckling, initiation and propagation results. The value for G_{IIC} was chosen to represent a lower bound value based on initial fracture of a 45° plane under pure shear $(G_{IIC} = 2\sqrt{2}G_{IC})$. This value was subsequently confirmed to be similar to the value obtained by experimental characterisation [18]. As an example of

local buckling output from ABAQUS, figure 9 shows the critical buckling mode of the $[0/90_2]$ laminate obtained from linear eigenvalue analysis. The delamination area buckles with two half-wavelengths, which agrees with the experimental buckling mode shown in figure 7(a). However, due to contact with the base laminate, the experimental sub-laminate buckle forms with unequal amplitude for each of the half waves in the load direction, this contact problem is not captured by the linear FEA model as superposition of the base laminate and sub-laminate was not prevented. However, contact is modelled during the non-linear propagation analysis presented below.

Table 3. Cohesive element parameters in FE model for T700GC/M21 material.

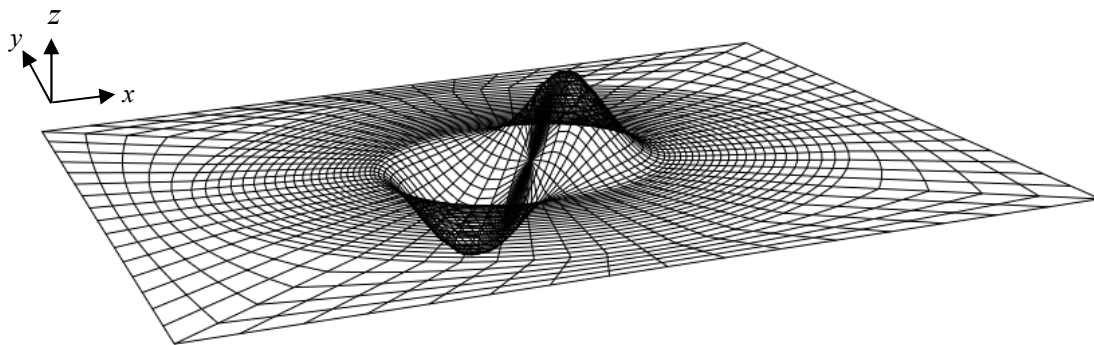| FE model parameters	Unit	Value
Stiffness	kN/mm^3	1000
Mode I strength	MPa	60
Mode II strength	MPa	90
Mode III strength	MPa	90
G_{IC}	J/m^2	550
G_{IIC}	J/m^2	1550
G_{IIIC}	J/m^2	1550

Figure 9. ABAQUS laminate buckling model for $[0/90_2]$ sub-laminate.

For the $[45_2]$ laminate, propagation initiates at about 60° to the load direction, as shown in figure 10(a). This is coincident with the experimental test, see figure 5(c) although intra-ply cracking subsequently forced experimental propagation to occur in the 45° direction, see figure 5(d). Figure 10(b) shows the delamination propagation of the $[0_2/90]$ laminate simulated by the ABAQUS model. As noted on figure 10 ABAQUS predicts that delamination initiation occurs when the nodes start to separate at 2838 µstrain. Propagation is predicted to occur transversely along a horizontal line through the centre of the delamination starting from a point on the perimeter of the delamination. Increasing applied strain in the ABAQUS model leads to propagation where a delamination area is formed as full elements fail (each element has four nodes which are all required to fail for the element to fail) as depicted in figure 10. The delamination then propagates in the horizontal direction, which is shown by the failure of cohesive elements.
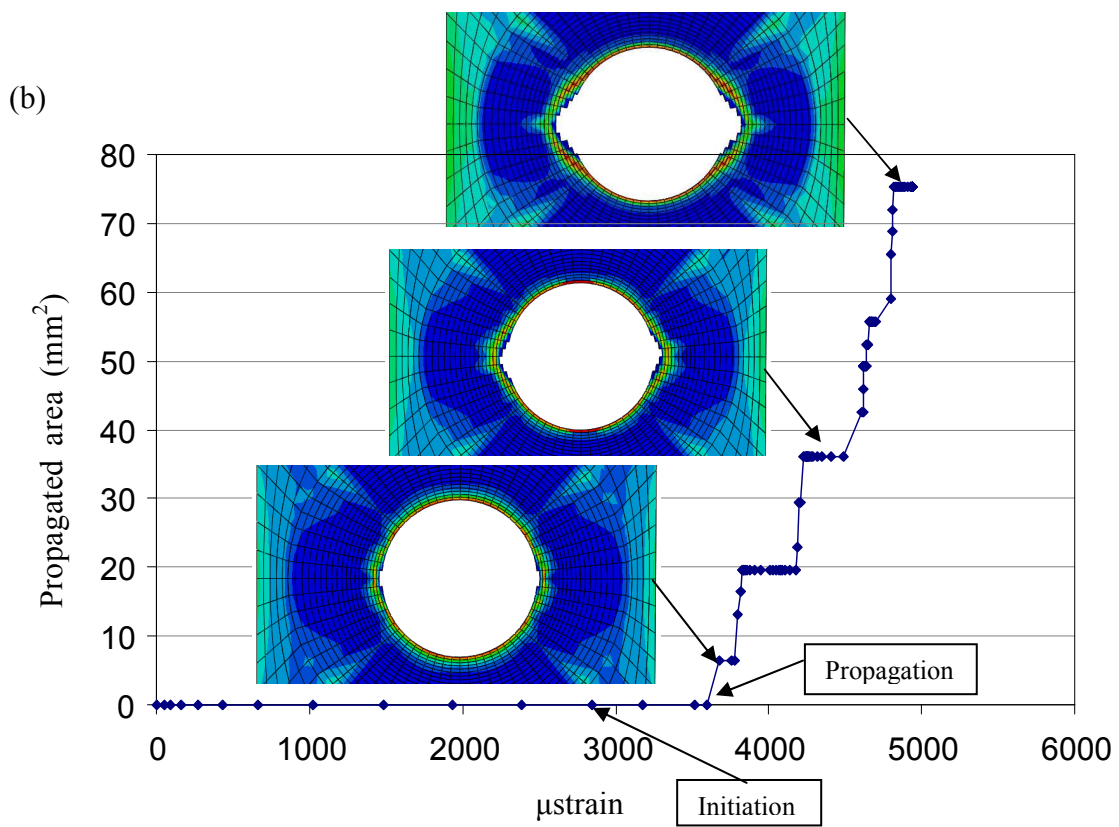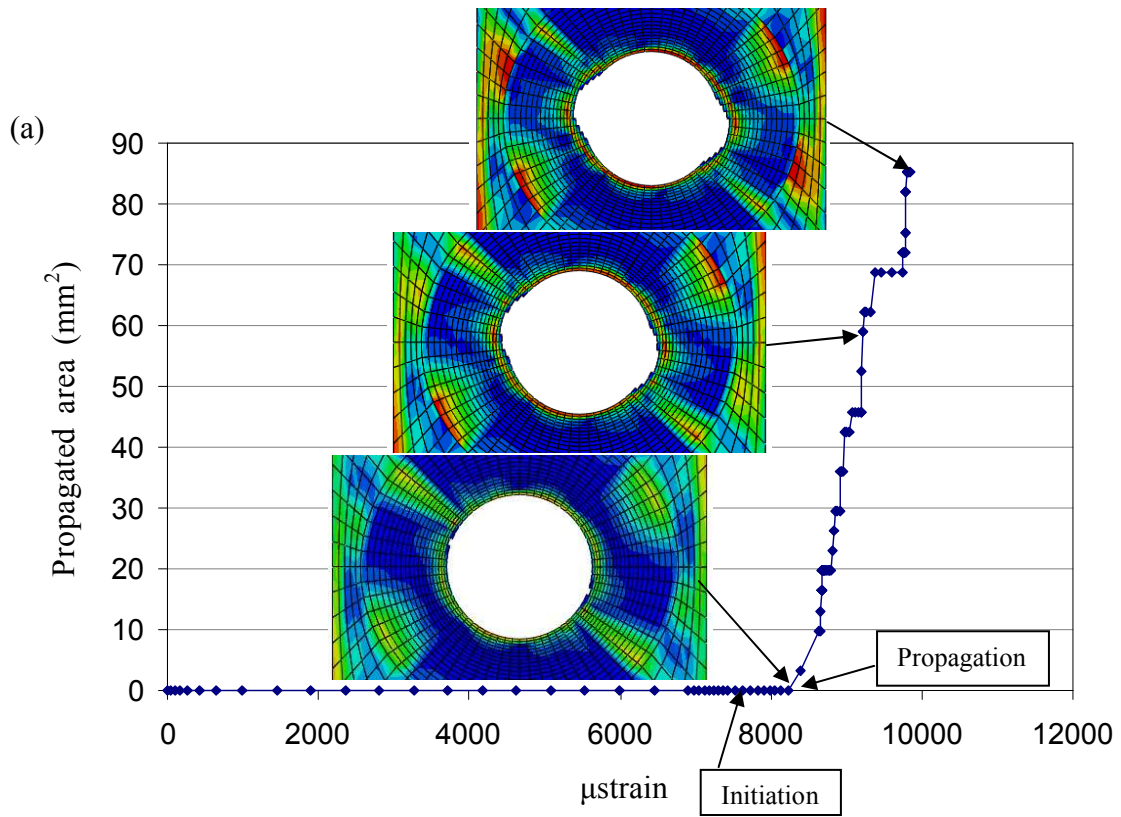
Figure 10. Propagation area as a function of applied strain for (a) the $[45_2]$ and (b) the $[0_2/90]$ laminate from ABAQUS. Load is applied vertically in the propagation images.

With the exception of the [45_2], [45/-45] and [0/45] laminates, where initiation strains were significantly unconservative, both the delamination initiation strain and subsequent direction of delamination propagation predicted by ABAQUS are in good agreement with the experimental tests.

As shown in table 2 in the previous section, propagation strains are between 5% and 65% higher than the initiation strains. For the cross-ply laminates [0_2], [90/0/90], [$0/90_2$], [$90_2/0$] and [$0_2/90$], these values are between 16% and 37%, whereas for the angle-ply laminates [45_2] and [45/-45], they are approximately 5%. The most asymmetric sub-laminate, [0/45], shows the highest difference of 65%. These variations are due to the mode mixity shown by different stacking sequences. Based on observation of the numerical simulations of delamination initiation and propagation, initiation in the case of the cross-ply sub-laminate is Mode I dominated. Once the nodes close to the delamination front are separated, the shear stress within the element is increased and more energy is required to fail the element in Mode II. For the angle-ply laminates, the delamination is initiated in Mode II and propagated by Mode II, so there is less energy required to fail the first element. The most complicated case is [0/45], where strong coupling occurs when the node is separated.

(d) Strip Model Results

Strip model local buckling and propagation threshold strain results are also given in table 2. Figure 11 shows a local buckling modeshape produced by VICONOPT [10] for the [$0/90_2$] sub-laminate which corresponds to the equivalent experimental (figure 7) and FEA (figure 9) local buckling modeshapes. VICONOPT does not take into account contact between the sub-laminate and base and hence does not produce the unequal half-wave amplitudes seen in the experiments, such as the [$0/90_2$] experiment, (note the number of contours on each half-wave of the buckle in figure 5(a)) where sub-laminate and base contact occurs. However, a comparison of Strip model and experimental results in table 2 suggest that contact between the sub-laminate and base during local buckling has limited influence on the accuracy of the buckling strain predictions.
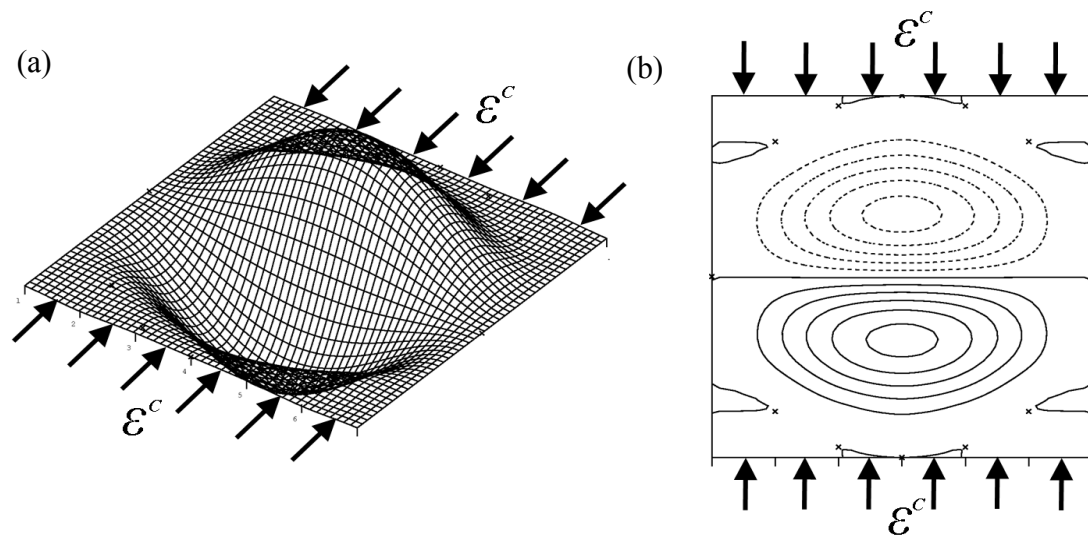

Figure 11. Local buckling modes obtained by VICONOPT for the [$0/90_2$] laminate. (a) 3D representation of the modeshape and (b) plan-view.

In general, propagation strains produced by the model are in agreement with both experimental and FEA results. The only exceptions to this being the [$0_2/90$] and [0/45]

sub-laminates which display, respectively, local-global interaction and full elastic coupling which are not captured by the strip model and the [45_2] and [45/-45] laminates for which the Strip model gives considerably more accurate predictions of experimental propagation initiation than does the FEA. However, for the [0_2/90] case, as noted in §4, local strains detected by the DIC in the areas into which propagation subsequently occurred were equal to the strains predicted by the Strip model.

4. Discussion

In the case of the [45_2], [$0/90_2$], [0_2/90] and [0/45] sub-laminates experimental buckling occurred without adhesion and hence all buckling strain results are well correlated. The [0_2], [45/-45], [90/0/90] and [90_2/0] sub-laminates suffered from residual adhesion between the base laminate and sub-laminate, the analytical models do not account for this and hence in these cases local buckling results are not well correlated with those from the experiments. Such adhesion did not seem to affect accuracy of either the FEA or the Strip model in predicting threshold strains. This is because, provided the PTFE region is eventually released, similar amounts of strain energy are developed. Other phenomena such as (i) contact between sub-laminate and base during local buckling, (ii) intraply cracking and (iii) propagation at multiple interfaces did not seem to affect the accuracy of the model, though in the latter case this is not unexpected as growth initiates at a single interface and does not spread to other interfaces until this has occurred. Note in particular that surface ply cracking the [0_2], [45_2] and [90_2/0] laminates did not appear to affect propagation strain predictions or growth direction as there was minimal stiffness and energy stored transverse to the fibre direction in these sub-laminates.

As in §3(b), some coupons demonstrated global bending. For example, figure 6 displays global buckling as a large change in gradient of the strain gauge curves between 100 and 140 kN indicating a change in stiffness. For most cases in table 2 interaction between local and global buckling modes has little affect on threshold strain. However, this is not true of the [0_2/90] coupon which has a considerable amount of axial stiffness its delaminated sub-laminate. Following buckling of the sub-laminate, the bending stiffness of the [0_2/90] laminate was considerably reduced and hence bending of the base occurred at a level of applied strain that was significantly lower than for other laminates. This is demonstrated by comparison of figure 5(b) showing limited global deformation (wide outer contours) of the [45_2] laminate and figure 8(b) showing significant global deformation (tight outer contours) in the [0_2/90] laminate at an equal level of load. The large out-of plane deformations displayed by the [0_2/90] caused a considerable local increase in compressive strain around the perimeter of the local buckle (see figure 12) that was not detected in the (far-field) strain measurements collected by the strain gauges. Figure 12 shows that the local strain in the region into which the delamination grows at initiation is approximately equal to the strip model prediction. In the case of the [0_2/90] laminate a large area has local strain greater than the threshold strain and hence propagation continues at a significant rate with increasing applied displacement. However, if the area into which propagation could occur is small (i.e. a very localised area with strain above threshold for the laminate) then growth will not occur as swiftly. Hence interaction between local and global buckling can have an effect on the rate at which propagation occurs and in cases where the areas of local strain above the threshold are very localised they are unlikely to be critical provided the far-field strain remains below the threshold strain. An example of this is the [0/45] laminate, although in this case the propagation

is also likely to have been influenced by the local post-buckling modeshape of the fully coupled sub-laminate which displays bend-twist coupling and is both asymmetric and unbalanced.

Note that for the purpose of optimum laminate design the results of table 2 indicate that delaminations creating sub-laminates containing $\pm 45^o$ angle plies are damage tolerant; in other words they display the greatest strength. Whereas, delaminated sub-laminates containing 0° plies are not damage tolerant. These observations are easily apparent from application of the model in the context of optimum design.

The initiation of damage, predicted by FEA is generally closer to the experimental propagation values than the FEA propagation strains. Use of the latter would give a prediction of propagation that is up to 85% higher than the experimental value. For all but the $[0_2/90]$ and $[0/45]$ cases considered above, the Strip model actually gives better agreement with experimental values than FEA initiation. This may be due to the inadequacy of the mixed mode formulation of equation (2.20) to capture all combinations of mode mixity.
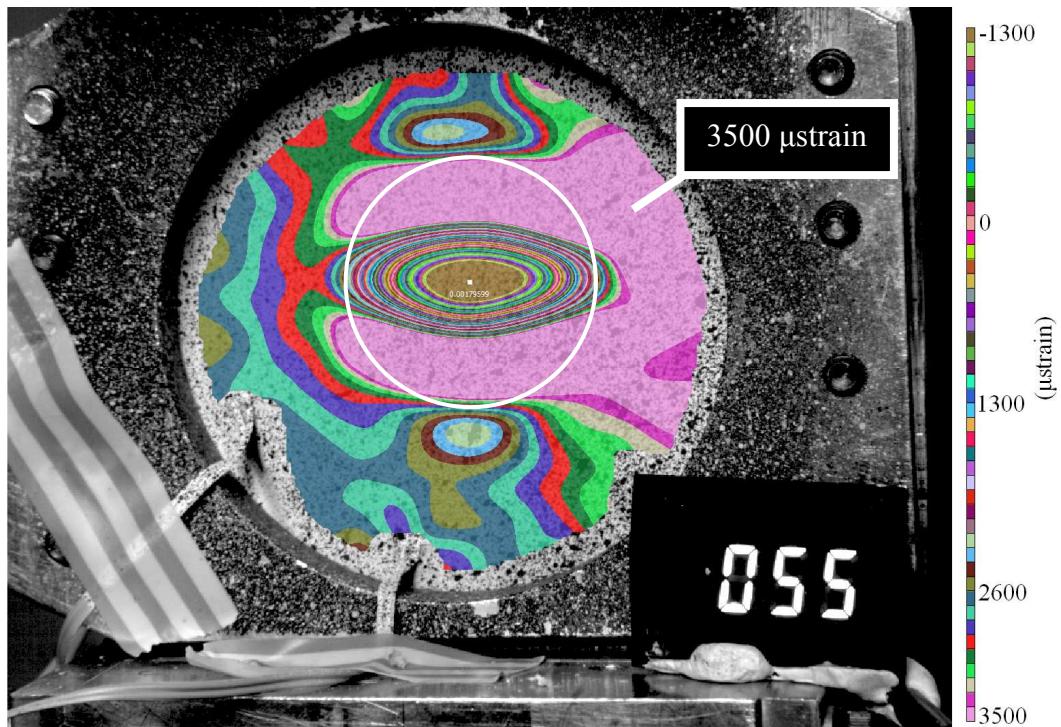

Figure 12. DIC image of the $[0_2/90]$ coupon showing the local *x*-strain (vertical) distribution at initial propagation with a 39mm circle highlighting the position of the original delamination. The applied load of 55kN corresponds to an average applied strain of 2670 µstrain.

5. Conclusions

New developments of a simple and efficient Strip model for predicting the threshold propagation strain of compressively loaded, delaminated composites have been presented. The accuracy and efficiency of the model make it well suited to application in optimum ply-stacking algorithms designed to maximise laminate strength. Indeed, a comparison of results with those from Finite Element Analysis and experimental compression tests indicate that, in most cases, the Strip model can conservatively predict the strain at which delamination propagation occurs to within 10% of

experimental values and 11% of FEA initiation values. The quoted accuracy of the model is true for sub-laminates displaying a range of anisotropy, including 90° ply dominated sub-laminates, subject to the following conditions: (i) the thin-film assumption made in the modelling methodology must hold and (ii) full elastic coupling effects must not play a significant role in the post-buckling of the sub-laminate. Non-linear FEA prediction of propagation using cohesive elements was shown to be significantly inaccurate in some cases, although initiation values gave reasonable agreement.

Future work should consider the implications of full elastic coupling in the sub-laminate and the interaction between local and global bucking, particularly if global buckling occurs before initial propagation.

Acknowledgements

References

1. Brewer, J.C. & Lagace, P.A. 1988 Quadratic Stress Criterion for Initiation of Delamination, *J. Compos. Mater.* **22,** 1141-1155.
2. Riccio, A., Caramuzzino, F. & Perugini. P. 2001 Embedded delamination growth in composite panels under compressive load. *Composites: Part B*. **32**, 209-218.
3. Shen, F., Lee, K.H. & Tay T.E. 2001 Modeling delamination growth in laminated composites. *Comp. Sci. Tech*. **61**, 1239-1251.
4. Suemasu H. & Kumagai T. 1998 Compressive behavior of multiply delaminated composite laminates Part 2: Finite Element Analysis, *AIAA J.* **36**(7), 1286-1290.
5. Rhead, A.T. & Butler, R. 2009 Compressive static strength model for impact damaged laminates. *Compos. Sci. Technol*. **69**, 2301-2307.
6. Chai, H., Babcock, C.D. & Knauss, W.G. 1981 One dimensional modelling of failure in laminated plates by delamination buckling. *Int. J. Solids Struct.* **17**, 1069–1983.
7. Chai, H. & Babcock, C.D. 1985 Two-dimensional modelling of compressive failure in delaminated. *J. Compos. Mater.* **19**, 67–98.
8. Butler, R., Almond, D.P., Hunt, G.W., Hu, B. & Gathercole, N. 2007 Compressive fatigue limit of impact damaged composite laminates. *Composites: Part A* **38**, 1211–1215.
9. Hunt, G.W., Butler, R., Almond, D.P. & Wright, J.E. 2004 Nonlinear modeling of delaminated struts. *AIAA J.* **42** (11), 2364–2372.
10. Williams, F.W., Kennedy, D., Butler, R. & Anderson, M.S. 1991 VICONOPT: program for exact vibration and buckling analysis or design of prismatic plate assemblies. *AIAA J.* **29**,1927–1928.
11. Wittrick, W.H. & Williams, F.W. 1973 Buckling and vibration of anisotropic or isotropic plate assemblies under combined loadings. *Int. J. Mech. Sci.* **16**, 209–239.
12. Anderson, M.S., Williams, F.W. & Wright, C.J. 1982 Buckling and vibration of any prismatic assembly of shear and compression loaded anisotropic plates with an arbitrary supporting structure. *Int. J. Mech. Sci*. **25** (8), 585–596.
13. Rhead, A.T, Butler, R. & Hunt G.W. 2008 Post-buckled propagation model for compressive fatigue of impact damaged laminates. *Int. J. Solids. Struct.* **45**(16), 4349–61.
14. Tay T.E. 2003 Characterisation and analysis of delamination fracture in composites: An overview of developments from 1990 to 2001. *ASME Appl. Mech. Rev.* **56(**1), 1-31.
15. ABAQUS, 2009. ABAQUS Analysis User's Manual 2009, Version 6.9. Dassault Systèmes Simulia Corp., Providence, RI, USA.
16. Benzeggagh, M. L. & Kenane M. 1996 Measurement of Mixed-Mode Delamination Fracture Toughness of Unidirectional Glass/Epoxy Composites with Mixed-Mode Bending Apparatus. *Comp. Sci.e and Tech.* **56**, 439–449.

17. Greenhalgh E. & Singh S. 1999 Investigation of the failure mechanisms for delamination growth from embedded defects. In *Proc. 12th Int. Conf. On Composite Materials (ICCM-12), 5-9 July Paris, France*.
18. Kinawy, M., Butler R. & Hunt G. W. 2011 Bending strength of delaminated aerospace composites. *Phil. Trans. R. Soc. Lond. A.* (Submitted).